

Phys-3D: Physics-Constrained Real-Time Crowd Tracking and Counting on Railway Platforms

Bin Zeng¹, Johannes Künzel^{1,2} ^a, Anna Hilsmann² ^b and Peter Eisert^{1,2} ^c

¹Visual Computing Group, Humboldt University Berlin, Unter den Linden 6, 10099 Berlin, Germany

²Fraunhofer Institute for Telecommunications, Heinrich Hertz Institute, HHI, Einsteinufer 37, 10587 Berlin, Germany
{johannes.kuenzel, peter.eisert}@hu-berlin.de, anna.hilsmann@hhi.fraunhofer.de

Keywords:

Crowd Counting, Multi-Object Tracking, DeepSORT, YOLO, Depth Estimation

Abstract:

Accurate, real-time crowd counting on railway platforms is essential for safety and capacity management. We propose to use a single camera mounted in a train, scanning the platform while arriving. While hardware constraints are simple, counting remains challenging due to dense occlusions, camera motion, and perspective distortions during train arrivals. Most existing tracking-by-detection approaches assume static cameras or ignore physical consistency in motion modeling, leading to unreliable counting under dynamic conditions. We propose a physics-constrained tracking framework that unifies detection, appearance, and 3D motion reasoning in a real-time pipeline. Our approach integrates a transfer-learned YOLOv11m detector with EfficientNet-B0 appearance encoding within DeepSORT, while introducing a physics-constrained Kalman model (Phys-3D) that enforces physically plausible 3D motion dynamics through pinhole geometry. To address counting brittleness under occlusions, we implement a virtual counting band with persistence. On our platform benchmark, MOT-RailwayPlatformCrowdHead Dataset (MOT-RPCH), our method reduces counting error to 2.97%, demonstrating robust performance despite motion and occlusions. Our results show that incorporating first-principles geometry and motion priors enables reliable crowd counting in safety-critical transportation scenarios, facilitating effective train scheduling and platform safety management.

1 INTRODUCTION

Real-time estimation of passenger density and movement on railway platforms is essential for safe and efficient train operation, as anticipating the number and distribution of waiting passengers enables adaptive dispatching and proactive safety management (Schneider et al., 2021; Zhang et al., 2024; Ge et al., 2025). Traditional platform surveillance systems rely on static cameras that provide limited coverage and are vulnerable to perspective distortion and occlusion. Therefore, we aim to enable real-time, onboard perception of platform crowds from a moving train. Fig. 1 shows typical frames from a tracked video se-

quence showing stable identity tracking and real-time counting results.

However, a moving camera comes with its own specific challenges, as for instance detection under severe perspective shifts and mutual occlusions. Distant heads rapidly scale up as the train approaches, and dense crowding often causes extensive overlap among passengers. Full-body detectors (e.g., YOLO variants) suffer degraded performance due to motion blur, heavy overlap, and partial visibility, leading to instability and missed detections (Kaur and Singh, 2024; Khan et al., 2020; Al-Ghanem et al., 2024; Zhang et al., 2020; Li et al., 2023). To mitigate these effects, we adopt a head-based detection strategy that leverages the greater visibility and stability of head regions in crowded scenes. We therefore fine-tune a YOLOv11m detector using two-

^a  <https://orcid.org/0000-0002-3561-2758>

^b  <https://orcid.org/0000-0002-2086-0951>

^c  <https://orcid.org/0000-0001-8378-4805>

stage transfer learning. To enable the handling of extreme scale variation and perspective distortion, we extent on the publicly available dataset (CrowdHuman (Shao et al., 2018), Open Sensor Data for Rail 2023 (Tilly et al., 2023), Rail-Eye3D (Wallner et al., 2021)) by meticulously labeling our own domain-specific RailwayPlatform-CrowdHead dataset.

A further challenge arises from ego-motion during the train’s approach. Classical multi-object tracking (MOT) models such as constant-velocity or constant-acceleration Kalman filters (Dai et al., 2022; Alkandary et al., 2025) often misinterpret camera-induced apparent motion as target motion, leading to physically inconsistent trajectories and frequent identity switches. To address this, we propose a physics-constrained model, termed Phys-3D, which explicitly incorporates the train’s ego-motion into the tracking state prediction. Operating within a perspective-aware coordinate system, Phys-3D decouples true pedestrian movement from camera-induced motion and applies geometric constraints to ensure physically coherent trajectories. This approach enhances temporal stability, reduces identity fragmentation, and preserves computational efficiency through a compact state representation.

Finally, even with stabilized tracks, converting dynamic trajectories into reliable passenger counts presents another layer of difficulty. Short occlusions, detection jitter, and temporary tracking losses can cause duplicate or missing counts when naïve crossing-line methods are applied. To ensure consistent measurement, we define geography-anchored virtual counting regions that correspond to real-world platform zones. By integrating a temporal persistence window, brief interruptions are smoothed out, yielding stable, region-specific counts despite visual disturbances.

Overall, the proposed framework jointly addresses occlusion-robust detection, ego-motion-aware tracking, and stable region-based counting, enabling accurate and reliable passenger analysis in real-world railway environments. In summary, our main contributions are:

- We design a real-time, end-to-end detect-track-analyze pipeline tailored for train approach, enabling forward-looking platform perception onboard the train.
- We propose a Phys-3D Kalman filter that incorporates physically grounded ego-motion constraints to address instability under strong perspective and camera motion.

- We release a new domain-specific dataset, RailwayPlatformCrowdHead, to facilitate head-based detection and crowd analytics from the train viewpoint.
- We demonstrate that combining physics-based motion modeling with deep visual representation yields accurate, stable, and efficient solutions for physically constrained vision tasks in transportation; for tracking-by-detection and DeepSORT foundations see (Zhang et al., 2023; Wojke et al., 2017; Xie and Yao, 2023).

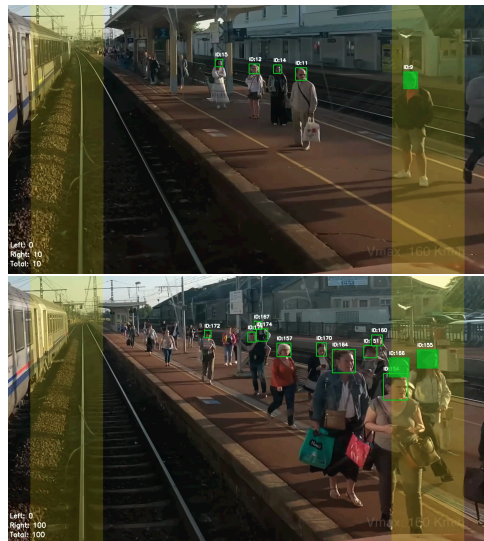


Figure 1: Two frames from a tracked video sequence. Each bounding box is annotated with a unique track IDs; the bottom-left overlay shows the unique-ID count from the virtual counting zone (yellow area).

2 RELATED WORK

Passenger detection and counting have evolved from handcrafted visual models to end-to-end deep learning frameworks. This section reviews related work in three domains: traditional methods, deep learning-based detection and tracking, and railway-specific crowd analysis.

Before deep learning dominated the field, crowd and passenger counting relied on handcrafted features and shallow models. Techniques such as Histogram of Oriented Gradients (HOG) and Hough transform were applied to detect passengers in bus or platform images (Khan et al., 2020; Chen et al., 2012). While computationally efficient, these classical approaches were

highly sensitive to illumination, perspective, and occlusion, resulting in poor generalization to crowded or dynamic scenes. Regression-based models that estimated global crowd density from low-level features (Zhang et al., 2016; Li et al., 2018) improved robustness but still failed to capture fine-grained individual localization.

Deep Learning for Crowd Detection and Counting. The advent of convolutional neural networks (CNNs) enabled the transition from feature engineering to feature learning. Early deep regression networks (Zhang et al., 2016; Li et al., 2018) predicted pixel-wise density maps, providing accurate crowd estimates in surveillance footage. However, density-based methods lose instance-level information required for multi-object tracking and identity consistency. Object detection frameworks such as Faster R-CNN and YOLO series (Redmon et al., 2016; Bochkovskiy et al., 2020; Jocher et al., 2023) addressed this issue by enabling explicit localization. They have since been adapted to head detection tasks (Shao et al., 2018), which are more robust in dense or occluded environments. Recent transformer-based detectors further improved long-range context modeling but typically require large datasets and high computational cost, limiting deployment in real-time transportation monitoring.

Multi-Object Tracking and Re-Identification. Multi-object tracking (MOT) extends detection into temporal association. Early online trackers combine Kalman filtering with Hungarian matching, achieving real-time performance (Bewley et al., 2016). Later works introduced appearance models and motion prediction enhancements, reducing identity switches in crowded scenarios (Wojke et al., 2017). Appearance-based re-identification (Re-ID) has become essential for maintaining consistent identities across frames (Ning et al., 2023). Networks based on EfficientNet and ResNet backbones extract discriminative embeddings that support robust association even under partial occlusions (Li et al., 2020; Luo et al., 2020). Despite these advances, most trackers assume a fixed camera and constant-velocity motion model, which breaks down in scenes with strong perspective variation or moving cameras—typical conditions for railway surveillance.

Crowd Counting in Transportation Scenarios.

Compared with generic crowd scenes, railway platforms present unique challenges: frequent partial occlusions, fast camera motion, and pronounced scale variation. While vehicle- or station-level passenger analytics have been studied (Di Gennaro et al., 2024; Tilly et al., 2023), most approaches rely on full-body detection, making them susceptible to mutual occlusion. Recent studies have highlighted the advantages of head-based counting (Shao et al., 2018), yet publicly available datasets remain limited and lack domain diversity for railway applications. The absence of unified benchmarks and physically grounded motion models further constrains reproducibility and cross-domain generalization.

In summary, while deep detection and tracking frameworks have achieved impressive accuracy in general crowd scenes, their performance degrades under railway-specific constraints: non-stationary cameras, narrow viewing angles, and dense human occlusion. Traditional constant-velocity Kalman filters fail to model perspective geometry, causing instability in trajectory estimation and erroneous counts. Moreover, few works explicitly address robust and unique counting, separating repeated entries and exits, from a physically constrained motion perspective. This motivates our work: an integrated detect-track-count system that combines head-based detection, appearance-aware re-identification, and a novel physics-constrained Kalman model designed to handle perspective distortion and physically plausible motion in real-time railway surveillance.

3 METHOD

This section presents our approach for accurate crowd counting on railway platforms. We propose a physics-constrained detect-track-count pipeline that combines YOLOv11m head detection, EfficientNet-B0-based ReID feature extraction, and a physics-constrained Kalman filter for robust real-time multi-object tracking.

Our key innovation is the Phys-3D physics-constrained tracker with internal states defined in 3D space instead of the 2D image plane, leveraging camera geometry and scene priors to stabilize identity consistency and achieve superior counting accuracy.

An overview of our proposed system is given in Fig. 2. Incoming video streams are processed in

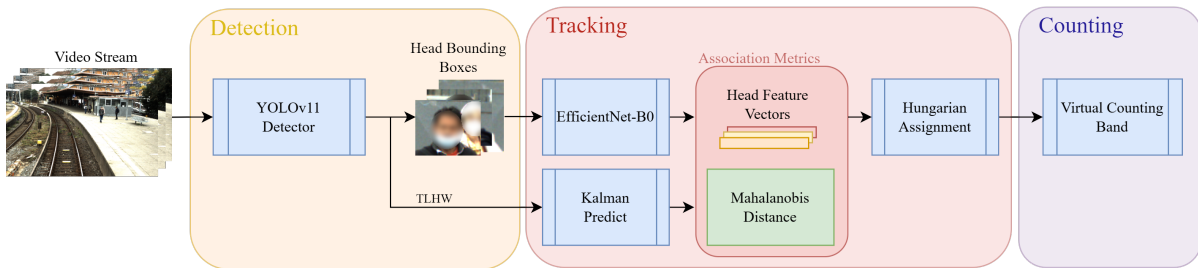


Figure 2: Overview of the proposed physics-constrained detect-track-count pipeline. The Phys-3D model integrates geometric and ego-motion priors to achieve stable identity tracking under camera motion.

three main stages: detection, tracking, and counting. In the detection stage, a head detector based on YOLOv11m localizes visible pedestrian heads, which provide more reliable cues than full bodies under dense occlusions.

The tracking stage extends the DeepSORT paradigm by combining visual appearance features from an EfficientNet-B0 encoder with a novel Phys-3D motion model that incorporates 3D geometric constraints and ego-motion priors. This enables physically consistent trajectory prediction even under strong perspective distortion and train deceleration, as Phys-3D incorporates camera geometry and ego-motion priors to distinguish between true pedestrian motion and apparent motion caused by train movement.

Finally, the counting stage aggregates stable tracks within defined platform regions using virtual counting zones with temporal persistence to handle brief occlusions and detection jitter.

The architecture is modular and runs in real time, allowing onboard crowd perception and analysis during train approach.

3.1 Head Detection and Encoding

Accurate detection underpins reliable multi-object tracking in dense crowds. On railway platforms, full-body detectors fail due to truncation, occlusion, and perspective-induced scale changes. We therefore focus on head detection, which remains stable and visible even in high-density scenes.

We employ YOLOv11m as the base detector to enhance robustness against occlusion and improve localization of small-scale head targets under strong perspective distortion by pre-training on the CrowdHuman dataset, followed by fine-tuning on our domain-specific RailwayPlatform-CrowdHead dataset. This adapts the model to the unique viewpoint and crowd characteristics of the train-mounted camera, substantially im-

proving localization stability under occlusion and motion blur. The bounding box of each detected head gets passed to the subsequent tracking module.

We extend the standard DeepSORT (Wojke et al., 2017) with an EfficientNet-B0 to encode detected heads as a 128-dimensional, L2-normalized embedding, enabling re-identification across frames and after temporary occlusions. EfficientNet-B0 was chosen for its favorable accuracy-efficiency trade-off, which allows real-time deployment on edge hardware and integration into multi-camera systems. The encoder is trained on a subset of our MOT-RPCH dataset containing 238 identities from seven video sequences. Comprehensive ablations on input resolution and normalization strategies guided the final configuration (128×128 input, aspect-ratio-preserving scaling). These robust head detections and appearance embeddings form the input to our physics-constrained tracking model, which leverages camera geometry and ego-motion priors to achieve consistent identity tracking under dynamic conditions.

3.2 Phys-3D: Physics-Constrained 3D Tracking

Standard tracking-by-detection frameworks such as DeepSORT combine appearance embeddings and 2D motion models effectively by assuming a constant velocity or constant acceleration of the bounding box motion and size in the image plane. While this works nicely for static video surveillance cameras, tracking might break down under camera ego-motion, strong perspective distortion and dense occlusions typical for railway platform scenes. In train-mounted cameras, apparent motion in the image plane is dominated by the train’s own motion and deceleration rather than by pedestrian dynamics, causing frequent trajectory drift and identity switches.

To overcome this limitation, we introduce Phys-3D, a physics-constrained 3D Kalman variant, which integrates camera geometry and ego-motion priors into the state prediction to achieve stable and physically consistent trajectory estimation.

We assume that the dominant motion of the pedestrians in the image plane is due to the ego-motion of the decelerating train along the track. Instead of modeling bounding box properties in image space, we define the Kalman state in 3D space, which is more constant. For example, a person’s head size typically does not change in 3D while the projection into the image plane varies drastically for a camera approaching the person.

In order to connect the 2D properties of detector and bounding box prediction with the 3D state, we assume a typical pinhole camera

$$\begin{aligned} x(t) &= c_x + f_x \cdot \frac{X}{Z(t)} \\ y(t) &= c_y + f_y \cdot \frac{Y}{Z(t)}, \end{aligned} \quad (1)$$

with f_x, f_y being the scaled focal length of the camera, (x, y) being the 2D center of the detected bounding box in image space, and (X, Y, Z) the 3D position of the person’s head with respect to the camera coordinate system. For a train approaching the platform on a relatively straight track and mainly in camera viewing direction, X, Y remain almost constant (up to the motion of the people on the platform) while the distance $Z(t)$ changes with the train’s position. If the train decelerates with a constant value, velocity and positional updates within a short interval Δt can be modeled as

$$\begin{aligned} Z_{k+1} &= Z_k + \dot{Z}_k \cdot \Delta t + \frac{1}{2} \cdot \ddot{Z}_k \cdot \Delta t^2 \\ \dot{Z}_{k+1} &= \dot{Z}_k + \ddot{Z}_k \cdot \Delta t \\ \ddot{Z}_{k+1} &= \ddot{Z}_k \end{aligned} \quad (2)$$

Assuming a constant head height (initialized with $H = 0.3m$) in 3D space, distance Z and detected bounding box height h can be related by

$$Z(t) = f_y \cdot \frac{H}{h(t)}. \quad (3)$$

With these relation between observable 2D quantities and the corresponding 3D values that can be derived through the pinhole camera model eq. (1), we can setup the Kalman state vector as

$$\mathbf{x}_{Phys3D} = [X, Y, H, Z, \dot{Z}, \ddot{Z}]^T. \quad (4)$$

This estimated state describes the 3D position of the person (X, Y, Z) with respect to the camera in the train. It assumes a more or less constant position on the platform (X, Y) as well as constant head height H , but a changing distance mainly due to the train’s ego motion, assuming a constant acceleration \ddot{Z} . By modeling the unknowns in 3D space, 2D motion trajectories are more constrained, leading to robust estimates even in case of occlusions.

3.3 Virtual Counting Band

Counting individuals in dynamic video streams is challenging due to occlusions, jitter, and identity switches that can cause duplicate or missed counts. To achieve robust aggregation, we introduce a virtual counting band that maps trajectories to defined spatial regions on the platform.

The band is parameterized by its horizontal boundaries (*Start, End*), expressed as proportions of the image width, and by a persistence threshold N defining the required number of consecutive frames a target must remain within the band to be counted. Each confirmed track maintains its state, including the number of consecutive in-band frames, whether it has already been counted, and its assigned platform side. Band membership is determined by testing whether the target’s horizontal position lies within the corresponding interval defined by *Start* and *End*. When a track remains within the band for at least N frames, it is counted once, and its ID is stored to prevent duplicate counts. At the end of a sequence, tracks partially satisfying the persistence condition can be conditionally included, and counts from both sides are aggregated to yield the final result. A visual illustration of the image regions can be found in Fig. 3.

4 EXPERIMENTS

This section presents comprehensive experimental evaluation of our Phys-3D physics-constrained tracking system. We demonstrate the effectiveness of our 3D geometric constraints and physics-based motion modeling for railway platform crowd counting applications. We start by introducing the used datasets for training and evaluation and giving implementation details to ensure reproducibility.



Figure 3: Virtual Counting Band Illustration. The diagram shows the virtual counting zones positioned near the left and right image borders. The band is defined by start and end boundaries as proportions of image width (Start=0.05, End=0.20), creating a buffer region that tolerates brief occlusions and detection jitter. A target is counted only when it remains continuously within the band for a preset number of frames, providing robust counting under challenging conditions.

4.1 Datasets

We constructed a comprehensive multi-modal dataset ecosystem for the training and the experiments. The following datasets have been used:

CrowdHuman The CrowdHuman dataset (Shao et al., 2018) is a large-scale, richly annotated, and highly diverse dataset for detector training. It contains roughly 470K human instances in 19,370 images.

Open Sensor Data for Rail 2023 The OSDaR dataset (Tilly et al., 2023) comprises multi-sensor sequences. We sampled 20 images with 180 instances from the RGB videos and manually annotated the headboxes.

RailEye3D The RailEye3D (Wallner et al., 2021) was originally intended for training systems targeting passenger safety during the boarding of the train and therefore features video sequences of cameras filming the side of the train. We manually annotated 320 images with 1,221 instances.

RailwayPlatformCrowd We also created our own dataset from publicly available YouTube-Videos covering 60 different railway platform scenes. From these we extracted 1,660 images and manually annotated 5,831 head bounding boxes.

MOT-RailwayPlatformCrowdHead Finally, in 27 video sequences from available YouTube-Videos comprising 24,788 frames, 89,087 bounding boxes, and 885 unique human head identities,

we annotated continuous head trajectories. The number of targets ranges from 3 to 124 and the sequences comprise different illumination, occlusion and crowd density conditions. The length of the sequences varies between a few seconds and tens of seconds.

4.2 Implementation Details

Detector The YOLOv11m detector pre-trained on the CrowdHuman dataset and finetuning on a combination of OSDaR (20 images, 180 instances), RailEye3D (320 images, 1,221 instances), and our RailwayPlatformCrowd (1,660 images, 5,831 instances) dataset. We trained using a SGD optimizer with lr=1e-2, momentum=0.937 and weight decay=5e-4, a cosine annealing scheduler and mixed precision. The training was conducted for 100 epochs for both stages. Further hyperparameters were kept the same as in the original implementation. During inference we used a confidence threshold of 0.5, IoU=0.7 and an input size of 640x640.

ReID model We trained the EfficientNet-B0 on 7 sequences with 238 tracked identities from our MOT-RailwayPlatformCrowdHead dataset with an input resolution of 128x128 with aspect-ratio preserving scaling and padding. The training uses a triplet loss with margin $\alpha = 0.5$, AdamW optimizer (lr=2 × 10⁻⁴, weight decay=1 × 10⁻⁴), OneCycleLR scheduling, mixed precision, and batch size 32.

Tracking We use DeepSORT with three Kalman state-space configurations. Association uses linear combination of Mahalanobis distance (motion) and cosine distance (appearance) with weight $\lambda = 0.5$. Cascaded matching prioritizes recently observed tracks. Gating thresholds: CV-8D uses standard DeepSORT thresholds; CA-12D uses stricter thresholds due to higher dimensionality; Phys-3D uses geometry-aware thresholds based on depth constraints.

Counting Virtual counting bands with Start=0.05, End=0.20 (relative to image width), persistence threshold N=2 frames. Per-ID deduplication and end-of-video compensation are applied. Final count uses maximum of left/right counts to avoid non-platform bias.

Camera Calibration: To enable accurate depth estimation and enforce the geometric constraints of the Phys-3D model, all video sequences were camera-calibrated to obtain intrinsic parameters, including focal length and principal point coordi-

nates. The calibration ensures consistent 3D-to-2D projection accuracy across varying camera resolutions and configurations in the MOT-RPCH dataset.

Evaluation For comprehensive evaluation, we select a representative subset of 20 video sequences from our MOT-RailwayPlatformCrowdHead dataset, spanning multiple resolutions (1536×864 to 2304×1296), frame rates (25, 29.97, 59.94 FPS), and target scales, totaling 18,548 frames, 647 identities, and 73,799 bounding boxes.

Metrics We evaluate using both standard multi-object tracking (MOT) and counting metrics. For tracking evaluation, we follow the CLEAR-MOT protocol (Bernardin and Stiefelhagen, 2008), adopting Multiple Object Tracking Accuracy (MOTA), Multiple Object Tracking Precision (MOTP), Identity F1 Score (IDF1), and Identity Switches (IDSW). Additionally, we report identity-based metrics, including Identity Precision (IDP), Identity Recall (IDR), and IDF1, as defined in (Ristani et al., 2016). For counting performance assessment, we employ regression-based metrics—Mean Absolute Error (MAE), Root Mean Squared Error (RMSE), Mean Absolute Percentage Error (MAPE), and Mean Error (ME)—to quantify discrepancies between predicted and ground-truth counts across all test videos.

4.3 Effectiveness of the Two-Stage Detector Training

We first pre-train on the larger general crowd dataset (CrowdHuman) and then fine-tune the network for the railway platform domain using the combination of our smaller, but domain-specific datasets. The performance of the head detector can be seen in Tab. 1. The results of the pretraining are shown in the first row of Tab. 1 and lead to a precision of $mAP_{50}=79.4\%$ and $mAP_{50-95}=54.7$, respectively. After fine-tuning, we achieve $mAP_{50}=98.0\%$ (+18.6 points) and $mAP_{50-95}=81.6\%$ (+26.9 points), highlighting the importance of the domain-specific training data.

4.4 EfficientNet-B0 ReID Model

To determine the optimal input resolution for our ReID model, we conduct a comprehensive ablation study comparing multiple input sizes under identical training settings. For the seven training sequences, we evaluate the speed-accuracy

trade-off across multiple resolutions. We evaluate six different input resolutions from 64×64 to 256×256 pixels in Fig. 4.

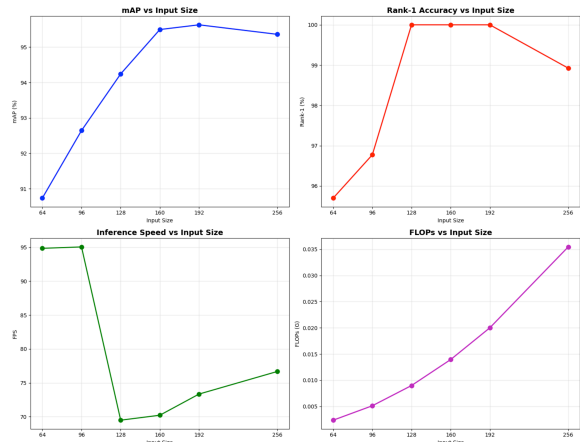


Figure 4: ReID Input Size Ablation Experiment Results

The results in Fig. 4 and Tab. 2 demonstrate clear performance improvements with increasing resolution, but with diminishing returns and increased computational cost. We observed an apparent FPS inversion at 128×128 , where larger inputs (e.g., 160×160) ran marginally faster, attributable to measurement artifacts: batch-size=24 placed 128×128 at a compute-communication tipping point, cuDNN’s Winograd path introduced extra transform overhead, and silent batch-size reductions at larger inputs increased effective GPU boost frequencies. This inversion does not change our conclusion that 128×128 lies on the accuracy–efficiency Pareto frontier (Rank-1=100% and $mAP=94.24\%$ at only 9 MFLOPs, leading to 69.5 FPS inference on a NVIDIA T4 GPU), and we therefore deploy 128×128 to ensure reproducibility and avoid confounders.

4.5 Comparative Analysis of Three State-Space Motion Models

To assess the role of different tracking approaches in MOT, we conduct a comprehensive comparison of three distinct tracking models: (i) the 8D constant-velocity baseline (CV-8D) with standard DeepSORT parameters, (ii) a 12D constant-acceleration model (CA-12D) with adjusted noise modeling for higher dimensionality, and (iii) our 3D physics-constrained model (Phys-3D) with specialized camera calibration and physics-based constraints. Both Kalman models 8D and 12D

Table 1: Performance of the YOLOv11m network. Upper row: after pre-training on the CrowdHuman Dataset. Lower row: fine-tuning results on the Custom Head Dataset.

Dataset	Images	Instances	Box(Precision)	Recall	mAP50	mAP50-95
CrowdHuman	4370	98568	0.862	0.715	0.794	0.547
Custom Human	600	4779	0.965	0.946	0.980	0.816

Table 2: ReID Ablation Experiment Results.

Input Size (pix)	mAP (%)	Rank-1 (%)	FPS	FLOPs (G)	Parameter quantity	Marginal benefits
64x64	90.74	95.7	94.8	0.002	206240	0
96x96	92.64	96.77	95	0.005	206240	+1.90 mAP
128x128	94.24	100	69.5	0.009	206240	+1.60 mAP
160x160	95.49	100	70.2	0.014	206240	+1.25 mAP
192x192	95.63	100	73.3	0.02	206240	+0.14 mAP
256x256	95.36	98.92	76.7	0.035	206240	-0.27 mAP

use an observation vector $\mathbf{z} = [x, y, a, h]$, with x, y being the center in pixels and a, h the aspect ratio and height of the bounding box, respectively. The evaluation was conducted on our evaluation dataset, MOT-RPCH. For the 8D model, a standard constant velocity is assumed, leading to the state vector

$$\mathbf{x}_{8D} = [x, y, a, h, \dot{x}, \dot{y}, \dot{a}, \dot{h}] \quad (5)$$

while the 12D model assumes a constant velocity, better capturing deceleration during arrivals:

$$\mathbf{x}_{12D} = [x, y, a, h, \dot{x}, \dot{y}, \dot{a}, \dot{h}, \ddot{x}, \ddot{y}, \ddot{a}, \ddot{h}] \quad (6)$$

We evaluate the three distinct tracking models, each configured solely with the adaptations necessary for its own state vector and dynamics, while holding the detector, ReID, association logic, and counting strategy exactly the same. Tab. 3 compares their counting performance under these settings.

Table 3: Counting performance comparison of the three models. Our Phys-3D approach clearly outperforms standard constant velocity or acceleration models.

Model	MAE	RMSE	MAPE(%)	ME
CV-8D	3.4	6.1514	14.592	1.4
CA-12D	2.4	4.5837	6.99	0.7
Phys-3D	0.9	1.3601	2.97	-0.2

The results indicate that counting accuracy in our platform scene is driven by physically plausible depth/scale evolution and robust association under occlusion. The CV-8D baseline, which assumes constant image-plane velocity, fails to capture the pronounced arrival deceleration and perspective-driven magnification,

leading to larger errors and a positive ME (double counting from ID fragmentation). CA-12D partially alleviates this by modeling acceleration, but its higher-dimensional kinematics without geometry/physics constraints remains noise-sensitive, yielding residual overcount ($ME > 0$). Phys-3D integrates a depth-aware state, an adaptive deceleration prior, and geometry-aware gating, which together enforce monotonic, bounded scale/depth evolution and suppress implausible re-associations. Combined with EfficientNet-B0 ReID, this reduces ID switches and re-entries through the counting band to achieve the lowest MAE/RMSE and MAPE. The small negative ME for Phys-3D suggests a conservative bias that prevents double counts at the cost of rare misses, which is preferable for deployment. Since detector, ReID, association, and counting settings are held fixed, these gains are attributable to the motion model and its physics-informed constraints rather than confounding factors.

4.6 Tracking and Counting Performance

We evaluate the counting performance of our proposed system on our evaluation dataset, MOT-RPCH. As described, the dataset provides a diverse set of weather conditions, number of persons and sequence lengths. As summarized in Tab. 4, Phys-3D achieves a MOTA of 67.19% and an IDF1 of 76.32%, with an average of only 24.5 identity switches. The model exhibits high precision (89.06%) and stable identity preservation under challenging railway platform conditions.

In terms of counting accuracy, as shown in the last row of Tab. 3, the Phys-3D system attains a Mean Absolute Percentage Error (MAPE)

of 2.97%, with MAE=0.9 and RMSE=1.36, validating the reliability of the physics-constrained 3D tracking approach for bidirectional passenger counting.

Table 4: Overall multi-object tracking performance of the Phys-3D model.

Metric	MOTA	IDF1	IDSW	Precision	Recall	FAF
Phys-3D	67.19%	76.32%	24.5	89.06%	77.43%	0.32

These results confirm the robustness and generalization capability of the Phys-3D framework in complex railway platform scenarios. Our Phys-3D model demonstrates strong performance across both tracking and counting tasks on the MOT-RPCH evaluation dataset.

4.7 Ablation Studies

To validate the effectiveness of individual components in our Phys-3D system, we conduct comprehensive ablation studies on the detector, ReID model, and counting method.

4.7.1 YOLOv11m Detector Ablation Study

We design our ablation study to examine the fine-tuned detector’s sensitivity to hyperparameters. We vary three key hyperparameters, input size, confidence threshold, and IoU threshold, according to Tab. 5 yielding 64 combinations.

Table 5: YOLO detection parameter values tested, yielding 64 combinations.

Confidence	0.3	0.5	0.7	0.9
IoU	0.3	0.5	0.7	0.9
Image Size	640	736	832	960

Through comprehensive evaluation across all combinations of parameters, we identify the optimal configuration that achieves the best balance between detection accuracy and inference speed, given in Tab. 6.

Table 6: Optimal YOLOv11m detector configuration.

Conf	IoU	Imgsz	mAP50	mAP50-95	Prec.	Recall	Inf. Time(ms)
0.3	0.3	736	0.9224	0.6871	0.9193	0.8707	16.86

The best performing parameter set balances precision–recall and feature resolution–compute trade-offs. A lower confidence threshold preserves more potential positives, an intermediate IoU threshold reduces duplicates without excessive suppression, and 736 px affords sufficient spatial detail for small heads while controlling cost. The configuration notably improves mAP50–95,

indicating robust performance across IoU thresholds and suitability for real-world deployment.

4.7.2 Ablation Study of the Counting Method

In addition, we evaluate the proposed Virtual Counting Band and its hyperparameters as shown in Fig. 3. The band introduces non-zero width and a persistence criterion to overcome line-crossing brittleness under jitter and occlusion. We focus on the start and end positions. We varied $Start \in \{0.05, 0.1, 0.15, 0.20, 0.3\}$ and $End \in \{0.15, 0.20, 0.25, 0.3, 0.35, 0.4\}$ with $Start < End$ for the virtual counting band configurations and systematically analyze the impact of start and end positions on counting performance. Our analysis reveals that the optimal configuration ($Start=0.05$, $End=0.2$) achieves exceptional counting accuracy with minimal systematic bias.

Table 7: Optimal virtual counting band configuration ($Start=0.05$, $End=0.2$).

Start	End	MAE	RMSE	MAPE(%)	ME
0.05	0.20	0.90	1.38	2.97	-0.20

Tab. 8 further contrasts average metrics for different counting strategies: line vs. band based crossing detection. The band dramatically outperforms the line based technique across MAE, RMSE, MAPE, and ME, demonstrating superior robustness and accuracy.

Table 8: Comparison of average counting metrics lines vs. zones.

Method	MAE	RMSE	MAPE(%)	ME
Line-crossing	31.28	43.66	93.43	-31.28
Counting zones	3.13	4.75	10.87	0.81

These results establish Phys-3D as a state-of-the-art solution for railway platform crowd counting, combining superior accuracy with real-time performance through physics-informed 3D tracking.

5 CONCLUSION

We presented a physics-constrained detect-track-count framework for real-time crowd analysis from a moving train. By integrating a geometry-aware Phys-3D motion model with head-based detection and appearance encoding, the system achieves stable identity tracking and accurate counting under dense occlusion and camera motion. Our experiments demonstrate that em-

bedding physical priors into multi-object tracking substantially improves robustness and interpretability in dynamic railway environments. We also demonstrated, that these priors are far more effective than merely increasing the complexity of the kinematic model.

The precise crowd counting capability provides multi-dimensional insights for railway station management, such as real-time safety and density management, operational efficiency and scheduling as well as capacity planning and infrastructure development. Accurate passenger counting serves as a foundation for higher-level analytics. Finally, future work will extend our approach to multi-camera fusion and domain adaptation for broader transportation scenarios.

Limitations and Future Directions While the Phys-3D framework demonstrates robust tracking and counting performance, our current dataset does not include extreme conditions such as nighttime illumination or adverse weather. Expanding data collection to encompass diverse environmental and operational scenarios would strengthen model generalization and robustness. In addition, domain randomization and simulation-based pretraining could further mitigate the data scarcity issue. Additionally, incorporating multi-modal sensing, such as LiDAR, radar, or thermal imaging, can enhance all-weather reliability and improve target discrimination in challenging visual conditions.

ACKNOWLEDGEMENTS

This work was partly funded by the German Federal Ministry for Economic Affairs and Energy (DeepTrain, grant no. 19S23005D).

REFERENCES

- Al-Ghanem, W. K., Qazi, E. U. H., Faheem, M. H., and Quadri, S. S. A. (2024). Deep learning based efficient crowd counting system. *Computers, Materials and Continua*, 79(3):4001–4020.
- Alkandary, K., Yildiz, A. S., and Meng, H. (2025). A Comparative Study of YOLO Series (v3–v10) with DeepSORT and StrongSORT: A Real-Time Tracking Performance Study. *Electronics*, 14(5):876.
- Bernardin, K. and Stiefelwagen, R. (2008). Evaluating multiple object tracking performance: the clear mot metrics. *EURASIP Journal on Image and Video Processing*, 2008(1):1–10.
- Bewley, A., Ge, Z., Ott, L., Ramos, F., and Upcroft, B. (2016). Simple Online and Realtime Tracking. In *2016 IEEE International Conference on Image Processing (ICIP)*, pages 3464–3468.
- Bochkovskiy, A., Wang, C.-Y., and Liao, H.-Y. M. (2020). YOLOv4: Optimal speed and accuracy of object detection. In *arXiv preprint arXiv:2004.10934*.
- Chen, J., Wen, Q., Zhuo, C., and Mete, M. (2012). Automatic head detection for passenger flow analysis in bus surveillance videos. In *2012 5th International Congress on Image and Signal Processing*, pages 143–147.
- Dai, Y., Hu, Z., Zhang, S., and Liu, L. (2022). A survey of detection-based video multi-object tracking. *Displays*, 75:102317.
- Di Gennaro, G., Greco, C., Buonanno, A., Cuciniello, M., Amorese, T., Ler, M. S., Cordasco, G., Palmieri, F. A. N., and Esposito, A. (2024). HUM-CARD: A human crowded annotated real dataset. *Information Systems*, 124:102409.
- Ge, H., Yang, X., Fan, Z., Flammini, F., and Koshizuka, N. (2025). Simulation of emergency evacuation in large scale metropolitan railway systems for urban resilience. *arXiv preprint arXiv:2507.19545*.
- Jocher, G., Qiu, J., and Chaurasia, A. (2023). Ultralytics YOLO.
- Kaur, J. and Singh, W. (2024). A systematic review of object detection from images using deep learning. *Multimedia Tools and Applications*, 83(4):12253–12338.
- Khan, S., Yousaf, M. H., Murtaza, F., and Velastin, S. (2020). Passenger detection and counting for public transport system. *NED University Journal of Research*, XVII:35–46.
- Li, X., Wu, Y., Fu, Y., Zhang, L., and Hong, R. (2023). A lightweight bus passenger detection model based on YOLOv5. *IET Image Processing*, 17(14):3927–3937.
- Li, Y., Qin, Y., Xie, Z., Cao, Z., Jia, L., Yu, Z., Zheng, J., and Zhang, E. (2020). Efficient ssd: A real-time intrusion object detection algorithm for railway surveillance. In *2020 International Conference on Sensing, Diagnostics, Prognostics, and Control (SDPC)*, pages 391–395.
- Li, Y., Zhang, X., and Chen, D. (2018). Csrnet: Dilated convolutional neural networks for understanding the highly congested scenes. In *Proceedings of the IEEE conference on computer vision and pattern recognition*, pages 1091–1100.
- Luo, H., Jiang, W., Gu, Y., Liu, F., Liao, X., Lai, S., and Gu, J. (2020). A strong baseline and batch normalization neck for deep person re-identification. *IEEE Transactions on Multimedia*, 22(10):2597–2609.
- Ning, E., Wang, C., Zhange, H., Ning, X., and Tiwari, P. (2023). Occluded person re-identification with deep learning: A survey and perspectives. *arXiv preprint arXiv:2311.00603*.

- Redmon, J., Divvala, S., Girshick, R., and Farhadi, A. (2016). You only look once: Unified, real-time object detection. In *Proceedings of the IEEE conference on computer vision and pattern recognition*, pages 779–788.
- Ristani, E., Solera, F., Zou, R., Cucchiara, R., and Tomasi, C. (2016). Performance measures and a data set for multi-target, multi-camera tracking. *European Conference on Computer Vision*, pages 17–35.
- Schneider, A., Krueger, E., Vollenwyder, B., Thurnau, J., and Elfering, A. (2021). Understanding the relations between crowd density, safety perception and risk-taking behavior on train station platforms: A case study from Switzerland. *Transportation research interdisciplinary perspectives*, 10:100390.
- Shao, S., Zhao, Z., Li, B., Xiao, T., Yu, G., Zhang, X., and Sun, J. (2018). Crowdhuman: A benchmark for detecting human in a crowd. *arXiv preprint arXiv:1805.00123*.
- Tan, M. and Le, Q. V. (2020). EfficientNet: Rethinking Model Scaling for Convolutional Neural Networks.
- Tilly, R., Neumaier, P., Schwalbe, K., Klasek, P., Tagiew, R., Denzler, P., Klockau, T., Boekhoff, M., and Köppel, M. (2023). Open sensor data for rail 2023.
- Wallner, M., Steininger, D., Widhalm, V., Schoerghuber, M., and Beleznai, C. (2021). Rgb-d railway platform monitoring and scene understanding for enhanced passenger safety. In *Pattern Recognition. ICPR International Workshops and Challenges*. Springer International Publishing.
- Wojke, N., Bewley, A., and Paulus, D. (2017). Simple Online and Realtime Tracking with a Deep Association Metric. In *Proc. International Conference on Image Processing (ICIP)*, Beijing, China.
- Xie, T. and Yao, X. (2023). Smart logistics warehouse moving-object tracking based on yolov5 and deepsort. *Applied Sciences*, 13:9895.
- Zhang, J., Ai, Q., Ye, Y., and Deng, S. (2024). Dynamic flow analysis and crowd management for transfer stations: a case study of suzhou metro. *Public Transport*, 16(2):619–653.
- Zhang, Y., Tu, W., Chen, K., Wu, C. H., Li, L., Ip, W. H., and Chan, C. Y. (2020). Bus passenger flow statistics algorithm based on deep learning. *Multimedia Tools and Applications*, 79(39):28785–28806.
- Zhang, Y., Wang, T., and Zhang, X. (2023). Motrv2: Bootstrapping End-to-End Multi-Object Tracking by Pretrained Object Detectors. *arXiv:2211.09791 [cs]*.
- Zhang, Y., Zhou, D., Chen, S., Gao, S., and Ma, Y. (2016). Single-image crowd counting via multi-column convolutional neural network. In *Proceedings of the IEEE conference on computer vision and pattern recognition*, pages 589–597.

APPENDIX

Detailed Per-Video Results

This appendix provides the complete per-video performance results for the Phys-3D system across all 20 test videos.

Table 9: Complete Phys-3D Detailed Performance Results Across All 20 Test Videos

Video	MOTA	MOTP	IDF1	IDP	IDR	IDSW	Matches	FP	Misses	FAF	Precision	Recall	MT	PT	ML	LC	RC	TC	TV	MAPE
1	54.26	19.63	72.96	81.73	65.89	2	86	16	41	0.16	84.62	68.22	1	3	0	0	4	4	4	0
2	57.35	17.64	75.65	87.65	66.55	3	375	51	187	0.22	88.11	66.9	3	5	0	8	0	8	8	0
3	57.25	17.66	73.19	77.53	69.32	7	993	215	359	0.52	82.3	73.58	12	10	3	24	0	25	25	0
4	78.33	16.74	83.16	81.49	84.9	1	610	86	58	0.29	87.66	91.33	9	1	0	0	10	10	10	0
5	64.42	16.5	78.33	79.56	77.14	3	874	175	208	0.36	83.37	80.83	13	4	1	19	0	19	18	5.56
6	81.1	16.11	82.98	84.91	81.13	8	2440	196	319	0.29	92.59	88.47	13	3	0	16	0	16	16	0
7	53.72	19.9	63.01	75.52	54.06	15	1097	150	651	0.29	88.11	63.07	6	10	5	0	21	21	21	0
8	57.31	16.91	74.24	81.18	68.39	17	2522	473	1036	0.44	84.3	71.02	20	23	4	1	44	44	47	6.38
9	73.84	15.94	79.76	88.47	72.6	87	10968	537	3071	0.26	95.37	78.26	71	51	2	0	123	123	124	0.81
10	78.67	18.02	85.86	88.98	82.96	12	1517	123	243	0.19	92.55	86.29	14	5	0	19	0	19	19	0
11	71.41	19.41	76.45	80.95	72.43	35	2507	266	596	0.33	90.53	81.01	18	8	1	27	0	27	27	0
12	68.76	19.79	72.11	79.28	66.13	94	8403	766	2609	0.33	91.73	76.51	36	27	1	66	0	66	64	3.12
13	76.76	15.26	83.84	92.13	76.92	4	498	19	122	0.08	96.35	80.45	8	4	0	11	0	12	12	0
14	56.74	17.15	66.1	74.66	59.31	119	8217	1320	3819	0.7	86.33	68.58	34	58	7	0	100	100	100	0
15	62.28	17.2	71.93	78.18	66.62	16	1947	296	688	0.43	86.9	74.05	16	10	2	29	0	29	28	3.57
16	63.13	17.31	74.31	75.3	73.35	17	2850	602	694	0.48	82.65	80.51	21	11	0	0	31	32	32	0
17	72.73	15.43	82.94	84.76	81.2	11	1218	162	223	0.34	88.35	84.64	11	4	1	0	15	15	16	6.25
18	79.97	15.45	70.53	73.22	68.03	6	1119	81	173	0.12	93.28	86.67	3	3	0	6	0	6	6	0
19	75.37	17.63	84.94	89.28	81	5	1073	97	217	0.34	91.74	83.24	15	7	2	0	21	21	24	12.5
20	60.73	18.45	73.56	89.79	62.29	34	2859	174	1528	0.18	94.33	65.44	12	32	2	43	0	43	46	6.52
Avg.	67.21	17.41	76.29	82.23	71.51	24.80	2609	290	842	0.32	89.06	77.45	16.80	13.95	1.55	13.45	18.45	32.00	32.35	2.24

This table provides the complete per-video analysis of Phys-3D performance across all 20 test videos. The results demonstrate consistent performance across diverse scenarios, with videos showing varying crowd densities and tracking challenges. The average values shown in the main text are calculated from these detailed per-video results. Note: LC is left counting value, RC is right counting value, and TV is the true value representing the actual number of people in the video.

Complete YOLOv11m Detector Ablation Study Results

This section provides the complete results of the YOLOv11m detector ablation study across all 64 parameter combinations.

Table 10: Complete YOLOv11m Detector Ablation Study Results Across All 64 Parameter Combinations

No.	Conf	IoU	Imgsz	mAP50	mAP50-95	Precision	Recall	Inference_Time(ms)
1	0.3	0.3	640	0.9248	0.6749	0.9272	0.8741	13.18
2	0.3	0.3	736	0.9224	0.6871	0.9193	0.8707	16.86
3	0.3	0.3	832	0.8997	0.6545	0.9195	0.8238	21.79
4	0.3	0.3	960	0.8664	0.6144	0.8947	0.7786	29.42
5	0.3	0.5	640	0.9247	0.6748	0.9246	0.8745	14.63
6	0.3	0.5	736	0.9224	0.6869	0.9177	0.8712	18.18
7	0.3	0.5	832	0.8997	0.6543	0.9183	0.8243	23.32
8	0.3	0.5	960	0.8661	0.6143	0.9003	0.7736	31.44
9	0.3	0.7	640	0.9244	0.6744	0.9316	0.8652	14.44
10	0.3	0.7	736	0.9220	0.6865	0.9120	0.8717	18.05
11	0.3	0.7	832	0.8991	0.6538	0.9146	0.8242	23.43
12	0.3	0.7	960	0.8654	0.6137	0.8944	0.7741	31.53
13	0.3	0.9	640	0.9163	0.6677	0.9263	0.8364	14.46
14	0.3	0.9	736	0.9138	0.6801	0.9153	0.8334	18.22
15	0.3	0.9	832	0.8892	0.6468	0.9049	0.7986	23.60
16	0.3	0.9	960	0.8523	0.6041	0.8829	0.7413	31.55
17	0.5	0.3	640	0.9193	0.6734	0.9411	0.8603	14.23
18	0.5	0.3	736	0.9156	0.6851	0.9342	0.8540	18.05
19	0.5	0.3	832	0.8946	0.6539	0.9229	0.8212	23.41
20	0.5	0.3	960	0.8591	0.6133	0.9176	0.7569	31.51
21	0.5	0.5	640	0.9192	0.6733	0.9390	0.8605	14.51
22	0.5	0.5	736	0.9157	0.6850	0.9329	0.8545	18.18
23	0.5	0.5	832	0.8946	0.6538	0.9217	0.8216	23.38
24	0.5	0.5	960	0.8591	0.6132	0.9162	0.7571	31.30
25	0.5	0.7	640	0.9190	0.6730	0.9355	0.8611	14.33
26	0.5	0.7	736	0.9155	0.6847	0.9295	0.8549	18.25
27	0.5	0.7	832	0.8942	0.6534	0.9175	0.8217	23.39
28	0.5	0.7	960	0.8586	0.6129	0.9124	0.7574	31.17
29	0.5	0.9	640	0.9121	0.6675	0.9263	0.8364	14.30
30	0.5	0.9	736	0.9087	0.6796	0.9153	0.8334	18.11
31	0.5	0.9	832	0.8859	0.6475	0.9049	0.7986	23.56
32	0.5	0.9	960	0.8477	0.6050	0.8829	0.7413	31.20
33	0.7	0.3	640	0.9108	0.6706	0.9572	0.8399	14.28
34	0.7	0.3	736	0.9076	0.6832	0.9525	0.8340	18.18
35	0.7	0.3	832	0.8845	0.6512	0.9430	0.7956	23.38
36	0.7	0.3	960	0.8482	0.6107	0.9381	0.7276	31.67
37	0.7	0.5	640	0.9108	0.6706	0.9563	0.8401	14.35
38	0.7	0.5	736	0.9077	0.6831	0.9519	0.8343	18.09
39	0.7	0.5	832	0.8846	0.6511	0.9424	0.7959	23.61
40	0.7	0.5	960	0.8482	0.6107	0.9380	0.7276	31.68
41	0.7	0.7	640	0.9106	0.6703	0.9543	0.8402	14.11
42	0.7	0.7	736	0.9073	0.6829	0.9494	0.8343	18.11
43	0.7	0.7	832	0.8845	0.6510	0.9412	0.7960	23.57
44	0.7	0.7	960	0.8479	0.6105	0.9362	0.7278	31.16
45	0.7	0.9	640	0.9055	0.6664	0.9216	0.8402	14.08
46	0.7	0.9	736	0.9023	0.6791	0.9147	0.8345	18.11
47	0.7	0.9	832	0.8782	0.6466	0.9076	0.7961	23.62
48	0.7	0.9	960	0.8399	0.6046	0.8993	0.7284	30.99
49	0.9	0.3	640	0.8713	0.6544	0.9844	0.7534	14.30
50	0.9	0.3	736	0.8688	0.6671	0.9804	0.7481	18.09
51	0.9	0.3	832	0.8426	0.6350	0.9749	0.7002	23.52
52	0.9	0.3	960	0.8061	0.5970	0.9759	0.6277	31.56
53	0.9	0.5	640	0.8713	0.6544	0.9842	0.7534	14.30
54	0.9	0.5	736	0.8688	0.6671	0.9804	0.7481	18.09
55	0.9	0.5	832	0.8426	0.6349	0.9747	0.7003	23.44
56	0.9	0.5	960	0.8061	0.5970	0.9759	0.6277	31.06
57	0.9	0.7	640	0.8711	0.6543	0.9836	0.7534	14.21
58	0.9	0.7	736	0.8687	0.6671	0.9797	0.7481	18.11
59	0.9	0.7	832	0.8426	0.6349	0.9747	0.7003	23.42
60	0.9	0.7	960	0.8060	0.5970	0.9758	0.6277	31.07
61	0.9	0.9	640	0.8692	0.6529	0.9748	0.7535	14.23
62	0.9	0.9	736	0.8670	0.6659	0.9723	0.7481	18.14
63	0.9	0.9	832	0.8403	0.6334	0.9670	0.7005	22.99
64	0.9	0.9	960	0.8028	0.5945	0.9653	0.6278	29.96

Complete Virtual Counting Band Ablation Study Results

This section provides the complete results of the virtual counting band ablation study across all parameter combinations.

Table 11: Complete Virtual Counting Band Ablation Study Results Across All Parameter Combinations

Start	End	MAE	RMSE	MAPE(%)	ME
0.05	0.20	0.90	1.38	2.97	-0.20
0.05	0.15	1.15	1.75	4.07	-0.95
0.00	0.15	1.25	1.77	4.67	-0.15
0.10	0.20	1.40	2.10	5.28	-1.10
0.00	0.20	1.50	2.14	4.97	0.60
0.15	0.30	1.50	2.37	8.58	0.20
0.00	0.10	1.80	2.57	5.83	-1.60
0.10	0.25	1.80	2.68	6.94	0.30
0.20	0.30	2.05	2.89	9.66	-0.85
0.05	0.25	2.10	2.93	6.55	1.10
0.15	0.25	2.10	2.81	9.57	-1.30
0.20	0.35	2.40	3.44	10.61	1.10
0.10	0.30	2.45	3.68	8.55	1.65
0.10	0.15	2.60	3.65	9.81	-2.50
0.00	0.25	2.75	3.94	8.59	1.85
0.05	0.10	2.75	3.56	8.78	-2.55
0.05	0.30	2.85	4.46	8.56	2.45
0.15	0.35	2.85	4.42	11.16	1.95
0.30	0.40	3.05	4.17	15.38	-0.55
0.15	0.20	3.15	4.38	11.45	-3.05
0.20	0.25	3.50	4.93	12.89	-2.80
0.30	0.35	3.50	4.43	16.85	-3.40
0.00	0.30	3.60	5.53	10.81	3.20
0.10	0.35	3.90	6.43	11.85	3.30
0.20	0.40	4.15	6.43	16.10	3.35
0.05	0.35	4.30	7.44	11.85	4.10
0.15	0.40	4.65	7.55	16.81	4.15
0.00	0.35	5.00	8.54	13.79	4.80
0.10	0.40	5.80	9.62	17.90	5.50
0.00	0.05	5.95	7.77	18.77	-5.95
0.05	0.40	6.30	10.62	18.11	6.30
0.00	0.40	7.00	11.72	20.05	7.00
0.30	0.30	31.10	43.49	92.71	-31.10
0.05	0.05	31.30	43.69	93.55	-31.30
0.15	0.15	31.30	43.67	93.58	-31.30
0.10	0.10	31.35	43.74	93.66	-31.35

This comprehensive ablation study reveals the critical importance of virtual counting band configuration for accurate crowd counting. The results demonstrate that moderate-width bands (Start=0.05, End=0.20) provide optimal performance, while degenerate line settings (Start=End) cause catastrophic degradation due to sensitivity to jitter and transient detection loss. The study validates the effectiveness of the proposed virtual counting band approach over traditional line-crossing methods.

Comparison of ImageNet Performance and Model Complexity Across CNN Architectures

This section presents a comparative analysis of ImageNet performance and computational complexity across representative CNN backbones.

Table 12: ImageNet performance versus computational complexity across EfficientNet and other representative CNN architectures (Tan and Le, 2020).

Model	Top-1 Acc.	Top-5 Acc.	#Params	Ratio-to-EfficientNet	#FLOPs	Ratio-to-EfficientNet
EfficientNet-B0	77.1%	93.3%	5.3M	1.0×	0.39B	1.0×
ResNet-50	76.0%	93.0%	26M	4.9×	4.1B	11×
DenseNet-169	76.2%	93.2%	14M	2.6×	3.5B	8.9×
EfficientNet-B1	79.1%	94.4%	7.8M	1.0×	0.70B	1.0×
ResNet-152	77.8%	93.8%	60M	7.6×	11B	16×
DenseNet-264	77.9%	93.9%	34M	4.3×	6.0B	8.6×
Inception-v3	78.8%	94.4%	24M	3.0×	5.7B	8.1×
Xception	79.0%	94.5%	23M	3.0×	8.4B	12×
EfficientNet-B2	80.1%	94.9%	9.2M	1.0×	1.0B	1.0×
Inception-v4	80.0%	95.0%	48M	5.2×	13B	13×
Inception-ResNet-v2	80.1%	95.1%	56M	6.1×	13B	13×
EfficientNet-B3	81.6%	95.7%	12M	1.0×	1.8B	1.0×
ResNeXt-101	80.9%	95.6%	84M	7.0×	32B	18×
PolyNet	81.3%	95.8%	92M	7.7×	35B	19×
EfficientNet-B4	82.9%	96.4%	19M	1.0×	4.2B	1.0×
SENet	82.7%	96.2%	146M	7.7×	42B	10×
NASNet-A	82.7%	96.2%	89M	4.7×	24B	5.7×
AmoebaNet-A	82.8%	96.1%	87M	4.6×	23B	5.5×
PNASNet	82.9%	96.2%	86M	4.5×	23B	6.0×
EfficientNet-B5	83.6%	96.7%	30M	1.0×	9.9B	1.0×
AmoebaNet-C	83.5%	96.5%	155M	5.2×	41B	4.1×
EfficientNet-B6	84.0%	96.8%	43M	1.0×	19B	1.0×
EfficientNet-B7	84.3%	97.0%	66M	1.0×	37B	1.0×
GPipe	84.3%	97.0%	557M	8.4×	–	–

As shown in Table 12, EfficientNet-B0 achieves a favorable balance between accuracy and computational complexity. With only 5.3M parameters and 0.39 GFLOPs, it delivers competitive ImageNet performance while substantially reducing resource requirements. This efficiency-accuracy trade-off makes it an ideal backbone for real-time ReID tasks in multi-camera and edge computing environments.

MOT Evaluation Dataset: 20 Videos

For comprehensive evaluation of the multi-object tracking and counting system, we select a representative subset of 20 video sequences from the complete MOT-RPCH dataset. This benchmark covers diverse operational conditions, including multiple resolutions (1536×864 to 2304×1296), frame rates (25–59.94 FPS), and target scales (AvgH≈49 px). The evaluation set comprises 18,548 frames, 647 identities, and 73,799 bounding boxes, providing a robust basis for performance assessment using standard MOT and counting metrics.

Table 13: Twenty video sequences selected from MOT-RPCH for multi-object tracking and counting evaluation.

Video	Resolution	FPS	Duration (s)	Frames	Frame Range	BBox Count	Objects	MinH (px)	MaxH (px)	MinW (px)	MaxW (px)	AvgH (px)	AvgW (px)	Format
1	1920×1080	25	8.2	205	98–196	129	4	27.24	57.35	20.38	52.67	37.75	30.39	.mp4
2	1920×1080	25	11.44	286	41–267	565	8	20.19	86.36	16.63	69.53	40.08	31.74	.mp4
3	1920×1080	25	18.12	453	36–451	1359	25	14.64	153.88	16.36	106.39	52.36	41.48	.mp4
4	2304×1296	59.94	7.84	470	44–427	670	10	34.95	130.56	24.32	129.21	63.99	55.43	.mp4
5	2304×1296	59.94	11.29	677	73–639	1085	18	24.82	197.75	17.58	227.34	70.60	65.51	.mp4
6	2304×1296	59.94	11.18	670	2–666	2911	16	18.00	289.02	20.16	259.88	77.29	64.89	.mp4
7	2304×1296	59.94	10.59	635	38–615	1807	21	26.90	146.26	18.23	153.21	57.48	52.73	.mp4
8	1536×864	59.94	24.96	1496	146–1215	3575	47	11.61	121.28	9.15	123.57	38.45	35.60	.mp4
9	1536×864	59.94	35.64	2136	12–2038	17243	124	10.90	118.12	7.05	129.81	33.12	30.31	.mp4
10	1536×864	59.94	13.48	808	5–790	1804	19	16.99	147.95	11.01	149.34	36.14	32.12	.mp4
11	1536×864	59.94	13.85	830	1–811	3317	27	19.80	119.80	13.53	117.22	38.06	33.33	.mp4
12	1536×864	59.94	39.44	2364	13–2346	11474	64	16.06	125.98	12.54	160.40	37.65	34.86	.mp4
13	2304×1296	29.97	11.48	344	21–344	624	12	26.93	142.54	18.41	146.67	55.66	48.32	.mp4
14	2304×1296	59.94	33.38	2001	92–1988	12249	100	16.18	183.24	13.09	205.83	53.81	51.92	.mp4
15	1536×864	59.94	19.19	1150	343–1077	2651	28	12.78	104.00	9.62	119.77	37.33	34.88	.mp4
16	1536×864	59.94	24.07	1443	178–1443	3561	32	15.15	115.60	12.86	118.58	41.97	38.90	.mp4
17	1536×864	59.94	8.51	510	14–510	1494	16	20.40	120.98	14.72	120.92	43.05	38.02	.mp4
18	2304×1296	59.94	12.01	720	1–720	1303	6	30.38	204.36	21.60	222.35	66.81	57.20	.mp4
19	2304×1296	59.94	5.09	305	16–299	1341	24	24.39	167.54	20.14	154.06	56.02	52.94	.mp4
20	2304×1296	59.94	17.43	1045	53–1045	4637	46	14.33	116.91	10.62	131.26	44.73	43.78	.mp4
Total	–	–	337.19	18548	–	73799	647	20.13	142.47	15.40	144.90	49.12	43.72	–

ReID Training and Ablation Dataset: 7 Videos

We trained the ReID model using seven video sequences. This subset provides diverse appearance variations and sufficient identity samples for robust feature learning, comprising 6,240 frames and 238 tracked identities.

Table 14: Seven video sequences for ReID training and ablation studies.

Video	Resolution	FPS	Duration (s)	Frames	Frame Range	BBox Count	Objects	MinH (px)	MaxH (px)	MinW (px)	MaxW (px)	AvgH (px)	AvgW (px)	Format
1	1920×1080	25	7.24	181	67–166	437	8	22.44	103.24	17.95	87.47	46.75	36.23	.mp4
2	1920×1080	25	7.16	179	64–151	181	3	22.85	58.42	14.31	49.01	36.74	27.28	.mp4
3	2304×1296	59.94	11.54	692	51–664	1914	53	15.91	194.65	14.42	221.60	57.45	51.93	.mp4
4	2560×1440	59.94	6.99	419	90–419	905	18	12.72	127.42	10.28	117.93	26.46	24.48	.mp4
5	2560×1440	59.94	45.71	2740	1–2697	7415	93	10.84	122.27	8.69	127.90	29.51	29.76	.mp4
6	2304×1296	59.94	15.01	900	22–898	1171	9	26.70	214.66	21.27	179.46	68.55	55.99	.mp4
7	2304×1296	59.94	18.84	1129	1–724	3265	54	16.65	162.63	10.00	199.17	56.05	54.55	.mp4
Total	–	–	112.49	6240	–	15288	238	18.30	140.47	13.85	140.36	45.93	40.03	–